Available online at www.sciencedirect.com
ScienceDirect
Trans. Nonferrous Met. Soc. China 34(2024) 1745−1758
Transactions of Nonferrous Metals Society of China
www.tnmsc.cn

# 3D characteristics and growth behavior of Fe-rich phases in Al−Si−Fe−Mn alloys during melt holding

Dong-fu SONG[1,2], Yu-liang ZHAO[3], Yi-wang JIA[4], Xin-tao LI[1,5], Nan ZHOU[1], Kai-hong ZHENG[1], Wei-wen ZHANG[2]

1. Guangdong Provincial Key Laboratory of Metal Toughening Technology and Application, Institute of New Materials, Guangdong Academy of Sciences, Guangzhou 510650, China;
2. National Engineering Research Center of Near-net-shape Forming for Metallic Materials, South China University of Technology, Guangzhou 510641, China;
3. School of Mechanical Engineering, Dongguan University of Technology, Dongguan 523808, China;
4. College of Materials and Metallurgy, Guizhou University, Guiyang 550025, China;
5. Jiangxi Universal New Material Technology Co., Ltd., Shangrao 334499, China

Received 4 December 2022; accepted 15 June 2023

**Abstract:** The morphological evolution and growth behavior of Fe-rich phases in the Al−7.0Si−1.0Fe−1.2Mn alloy during melt holding were studied using scanning/transmission electron microscopy, thermodynamic calculations and synchrotron X-ray imaging. The results show that with a decrease in holding temperature, the Fe-rich phase underwent a morphological transformation from coarse star-like and polygonal structures to fine Chinese-script and coupled structures consisting of Chinese-script and polygonal shapes. The 3D structure of the star-like phase was composed of multibranched primary phases and irregular secondary phases; the coupled structure was composed of polyhedrons and dendrites; the Chinese-script phase was composed of dendrites. When the holding temperature was decreased, the number and volume fraction of Fe-rich phases were significantly reduced. A similar trend was also obtained for the largest volume particles and their connectivity. In situ synchrotron X-ray radiography results indicated that two types of primary Fe-rich phases were formed during the solidification process, and the smaller phase that remained in the melt could act as nucleation sites for the formation of the coupled eutectic structures.

**Key words:** holding temperature; Al−Si alloy; Fe-rich phase; 3D morphological evolution; synchrotron X-ray

## 1 Introduction

Aluminum alloys have been widely used in aerospace, automobile, railway, communications and electronics and other fields owing to their high specific strength and stiffness, good processability, ease of casting and corrosion resistance. Although aluminum production represents one of the largest greenhouse gas producers and is an energy-intensive industry [1−4], the infinite recyclability of the aluminum alloys [5,6] results in energy consumption and greenhouse gas emissions of only 4.7% and 5.0% of conventional metal-production processes, respectively [7]. Recycled alloys contain various impurities, such as Fe, Si, Cu, Zn, Sn and Mg, introduced from "dirty" aluminum alloys [1,8], among which Fe is prone to form Fe-rich intermetallic compounds in Al alloys due to its low solubility [9]. These intermetallic compounds, normally exhibiting a networked plate-like morphology, can separate the matrix and cause stress concentration during tensile testing, which is detrimental to mechanical properties of the alloy,

**Corresponding author:** Wei-wen ZHANG, Tel: +86-20-87112022, E-mail: mewzhang@scut.edu.cn
DOI: 10.1016/S1003-6326(24)66504-0

especially ductility [10−14].

Reducing the Fe content is an effective strategy to minimize these adverse consequences in recycled aluminum [15]. However, it is highly challenging and uneconomical to separate Fe from molten aluminum directly. In recent decades, many efforts have been made to remove Fe with an Fe-rich phase by ceramic filtration, electromagnetic sedimentation, centrifugal separation and gravity sedimentation [16−20]. MORAES et al [16] combined Mn addition, melt holding and ceramic filtration to separate primary Fe-rich particles, achieving an Fe removal rate of 83%. KIM et al [17] employed melt holding and centrifugation to reduce the Fe content in an Al−12Si−3.4Fe alloy, and the maximum Fe removal rate reached 82%. XIAO et al [21] reported an Fe removal rate of more than 90% by Mn doping and electromagnetic directional solidification. Gravity sedimentation has attracted increasing attention because it is a simple process and has wide application prospects. FLORES et al [22] studied the effects of holding temperature, Mn and Fe contents on the Fe removal rate during gravity sedimentation, and 80% of Fe was decreased at a higher Mn addition and a lower holding temperature. CAO and CAMPBELL [23] reported that a larger Mn/Fe ratio can result in a higher Fe removal rate under the same gravity sedimentation conditions, while BECKER et al [24] claimed that Cr addition is more suitable for Fe removal than Mn. Based on gravity sedimentation, ZHANG et al [25] proposed rotor stirring and argon blowing during melt holding, which significantly improved the Fe removal rate of Al−7Si−0.3Mg−0.56Fe−1.64Mn−0.51Cr. However, the addition of excessive Mn and Cr leads to the formation of a Mn-rich phase and a Cr-rich phase, thereby hindering further improvement in sedimentation efficiency [26,27]. In our previous works, we found that Mn doping combined with low-temperature insulation can not only reduce the Fe concentration but also promote the formation of Fe-rich phases with a fine, compact polygonal, Chinese-script morphology [28−30]. These Fe-rich phases can be divided into solid polyhedrons, hollow solid polyhedrons and multibranched hollow polyhedrons in a three-dimensional (3D) structure. It should be stressed that the gravity sedimentation approach is still focused on Fe removal and related parameters, but 3D morphological evolution of the Fe-rich phases involved in the sedimentation process still needs to be investigated.

Therefore, the objective of the present study is to reveal the morphological evolution and growth behavior of the Fe-rich phase in an Al−7.0Si−1.0Fe−1.2Mn alloy during melt cooling and holding. Synchrotron X-ray imaging was used to analyze the 3D structural characteristics and in situ growth process of the Fe-rich phase. The crystal structures of Fe-rich phases with different morphologies were identified by transmission electron microscopy (TEM). Thermodynamic calculations were carried out to analyze the phase transitions in Fe-rich compounds.

## 2 Experimental

### 2.1 Material preparation

The experimental alloys were designed based on commercially pure aluminum (99.7%), pure magnesium (99.9%), Al−20Si, A1−20Fe and Al−10Mn. Approximately 6 kg raw materials were melted in an electrical resistance furnace at (800±5) °C. After holding the temperature for 30 min, the temperature was decreased to (720±5) °C. Subsequently, approximately 20 g preheated (~250 °C) refining agent composed of a halogenated salt was added to the melt using a titanium bell jar. Finally, the slag was cleaned after holding the temperature for 30 min, and the melt was poured into a preheated (~250 °C) cylindrical mold with a diameter of 110 mm. To investigate the influence of holding temperature on the characteristics of Fe-rich phases, the prepared ingot was divided into several equal parts, and each ingot was remelted at (800±5) °C. The refining treatment was performed at (720±5) °C, and then the temperature was dropped to (615−680) °C. After holding at this temperature for 1 h, the melts were poured into preheated (~250 °C) rectangular molds with sizes of 30 mm × 200 mm × 150 mm.

### 2.2 Microstructural analysis

The chemical compositions of each ingot were measured by an optical emission spectrometer (SPECTRO-MAX). The initial compositions of the ingots were as follows: 6.87 wt.% Si, 1.02 wt.% Fe, 1.17 wt.% Mn, and 0.29 wt.% Mg and balanced Al. The specimens were intercepted at the same position (20 mm from the bottom) of the ingot by wire electric discharge cutting. After grinding, polishing and etching using 0.5 vol.% HF aqueous solution, the two-dimensional (2D) morphologies of each specimen were observed by scanning electron microscopy (SEM, Gemini SEM 300), and the chemical compositions of the Fe-rich phase were analyzed by energy dispersive spectrometry (EDS, OXFORD−7412). Transmission electron microscopy (TEM, FEI 3010, Philips microscope) was used to identify the type of Fe-rich phase. The equilibrium solidification phase diagram of the Al−7.0Si−1.0Fe−Mn alloy was constructed based on the Pan Aluminum 2016 database [31].

### 2.3 Synchrotron radiation X-ray computed tomography

The synchrotron X-ray tomography experiments were carried out on the BL13HB beamline of Shanghai Synchrotron Radiation Facility (SSRF), China. The experimental description can be found in detail in previous works [30,32]. The specimens were machined into rods with a diameter of 1 mm and fixed on a rotatable sample table. Subsequently, the specimens were placed on the optical path of a high-energy X-ray beam and rotated 180° at a constant speed, and 1200 projection images were obtained using a 2048 pixel × 2048 pixel CCD camera. The image resolution and exposure time were 0.65 μm/pixel and 0.3 s, respectively. The energy of the X-ray was 20 keV, and the distance between the specimens and the camera was 13 cm. Finally, PITER and Avizo$^{TM}$ softwares were used to recover and reconstruct the 3D structure of the Fe-rich phase, and the volume fraction, equivalent diameter ($D_{eq}$), sphericity ($\Phi$), mean curvature ($H$), connectivity ($I$) and surface thickness ($d$) were quantitatively characterized as shown in Ref. [33].

### 2.4 In situ observation and solidification analysis

In situ synchrotron X-ray radiography experiments were also conducted on the BL13W1 beamline. To characterize the growth behavior of Fe-rich phases, a programmable electrical resistance furnace was used to heat and cool the samples. The samples were thinned to 200−300 μm and sealed between two ceramic sheets. The samples were first heated to 750 °C at a rate of 30 °C/min, held at this temperature for 5 min, and then cooled at a cooling rate of 1 °C/min. When the temperature reached 675 °C, a continuous capture mode was initiated until 550 °C. The resolution and the exposure time of the images were 3.25 μm and 0.15 s, respectively. Image Pro-Plus software was used to reduce the background and analyze the growth behavior of the Fe-rich phase.

## 3 Results

### 3.1 Fe removal rate

Figure 1 shows the residual contents of Fe and Mn and the Fe removal rate in the alloy at different holding temperatures. With decreasing holding temperature, the contents of Mn and Fe decreased gradually (Fig. 1(a)), whereas the Fe removal rate increased (Fig. 1(b)). It is worth noting that the residual Fe content declined to 0.43%, and the Fe removal rate reached 57.8% when the melt holding temperature was 615 °C.

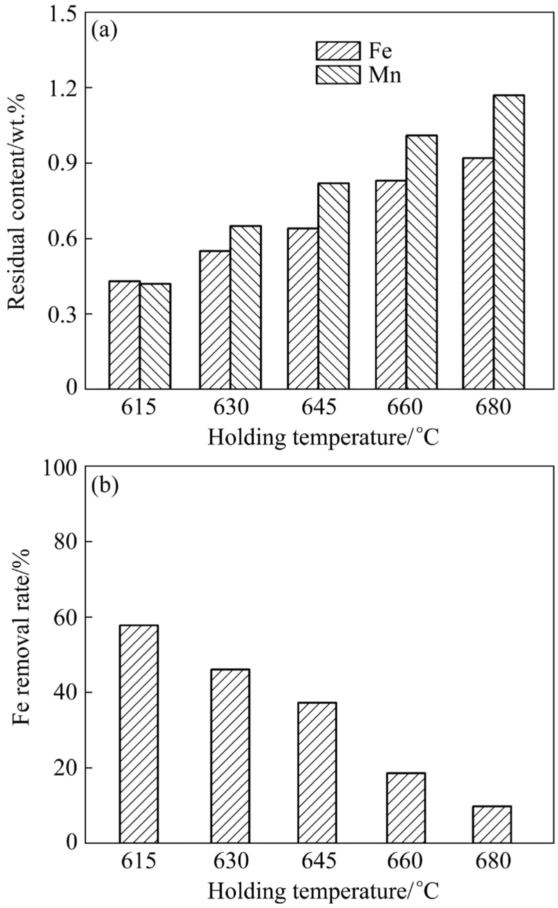


**Fig. 1** Residual contents of Fe and Mn (a) and Fe removal rate (b) of alloy at different holding temperatures

### 3.2 Microstructure

Figure 2 shows the SEM images of the Fe-rich phase in the alloy at different holding temperatures. The Fe-rich phase mainly exhibited coarse star-like and Chinese-script morphologies in the alloy at 680 °C. These Fe-rich phases were unevenly distributed and showed obvious microstructural segregation. When the holding temperature dropped from 660 to 645 °C, the segregation phenomenon did not significantly change, but the morphology of the Fe-rich phase was transformed into a regular polygon shape, while the area fraction of the Chinese-script phase significantly decreased (Figs. 2(b) and (c)). When the holding temperature was further reduced to 615 °C, the Fe-rich phases with fine granularity and Chinese-script morphologies were uniformly distributed, which greatly improved the microstructural uniformity of the alloy.

Figure 3 shows the high-magnification SEM images of typical Fe-rich phases in Fig. 2. With a decrease in melt holding temperature, both the amount and size of coarse primary Fe-rich phases decreased below 645 °C. As seen in Figs. 3(a) and (e), many coarse primary Fe-rich phases with sizes of approximately 60 μm appeared at 680 °C, and the size of these phases significantly decreased to a range of 15−20 μm at 615 °C. In addition, the morphology of the primary Fe-rich phase gradually changed from irregular star-like shape to regular

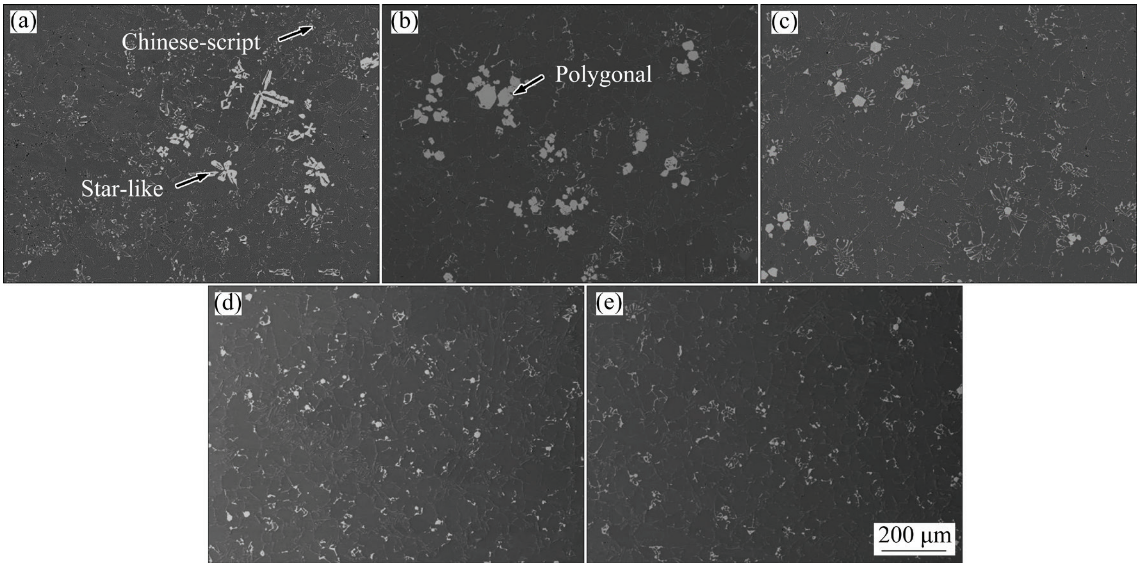


**Fig. 2** SEM images of Fe-rich phases in alloy at different holding temperatures: (a) 680 °C; (b) 660 °C; (c) 645 °C; (d) 630 °C; (e) 615 °C

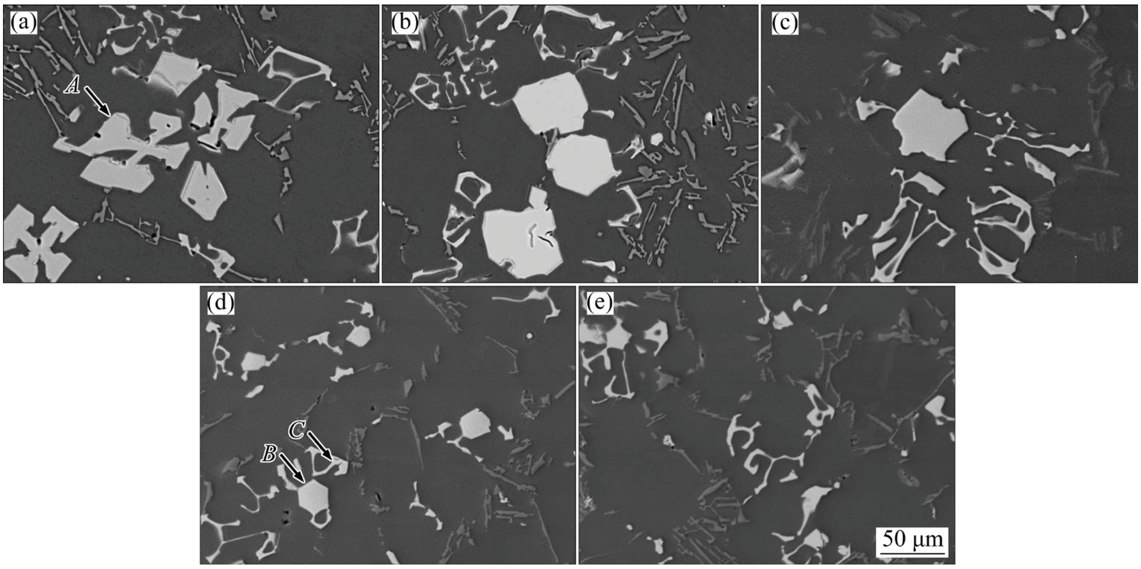


**Fig. 3** high-magnification SEM images of typical Fe-rich phases in alloy at different holding temperatures: (a) 680 °C; (b) 660 °C; (c) 645 °C; (d) 630 °C; (e) 615 °C

polygonal and Chinese-script shapes, and some polygonal particles were connected to the Chinese-script particles. The structure consisting of regular polygonal and Chinese-script phases is called a coupled structure [34]. Although the morphologies of the Fe-rich phases showed no obvious changes with holding temperature in the range of 615−630 °C, their sizes gradually decreased, and their densities significantly increased.

Table 1 shows the chemical compositions of the Fe-rich phases in Fig. 3 based on EDS analysis data. The chemical elements in the typical Fe-rich phases are Al, Fe, Mn and Si, which means that the constituent elements of primary and secondary Fe-rich phases are similar. However, the relative contents of Mn and Fe changed to a certain extent among different morphologies. For example, the Mn content of the star-like phases is close to that of the polygonal phases but higher than that of the closely connected Chinese-script phases, while the Fe content accordingly increases. The total content of (Mn+Fe) and molar ratio of (Mn+Fe)/Si are unchanged among the three different Fe-rich phases. The types of these Fe-rich phases with the above morphologies have been described in the previous work [28] and are consistent with $\alpha$-$Al_{15}(FeMn)_3Si_2$.

Figure 4 shows the SEM image and line scan of a typical coupled Fe-rich phase. Compared with the center of the polyhedron phase, the Mn contents in the Chinese-script phases and at the edge of the polygonal phases are significantly reduced, while their Fe contents are slightly increased. The thermodynamic calculations in Ref. [27] showed that the higher the Mn content in the Al−Si−Fe−Mn alloy is, the higher the formation temperature of the Fe-rich phase is. In other words, the formation of the polygonal Fe-rich phase in the center occurs prior to others, while the formation stage of the edge of the polygonal phases is close to that of the Chinese-script phase. Competitive growth between the secondary Fe-rich phases and $\alpha$(Al) leads to an irregular morphology and a coupled structure.

Figure 5 presents the bright field TEM images and selected area diffraction patterns (SADPs) of the two typical Fe-rich phases at holding temperature of 630 °C. The Chinese-script and polygonal phases are identified to have body centered cubic (BCC) structures with a lattice constant of 1.235 nm, which is consistent with $\alpha$-$Al_{15}(FeMn)_3Si_2$ [32]. The incident beam directions of the Chinese-script and polygonal Fe-rich phases are [111] and [100], respectively. The combined SADPs and EDS results further confirmed the crystal structures of Chinese-script and polygonal Fe-rich phases. There are some compositional differences between the two Fe-rich phases with different morphologies and various formation stages, which can be attributed to the microsegregation caused by different equilibrium solidification coefficients of Fe and Mn [35].

**Table 1** Chemical compositions of Fe-rich phases with typical morphologies

| Point in Fig. 3 | Morphology | Al | Si | Mn | Fe | Phase |
|---|---|---|---|---|---|---|
| *A* | Star-like | 60.55 | 10.50 | 18.31 | 10.64 | $\alpha$-$Al_{15}(FeMn)_3Si_2$ |
| *B* | Polygonal | 59.07 | 10.24 | 19.64 | 11.05 | $\alpha$-$Al_{15}(FeMn)_3Si_2$ |
| *C* | Chinese-script | 62.44 | 10.29 | 14.53 | 12.74 | $\alpha$-$Al_{15}(FeMn)_3Si_2$ |

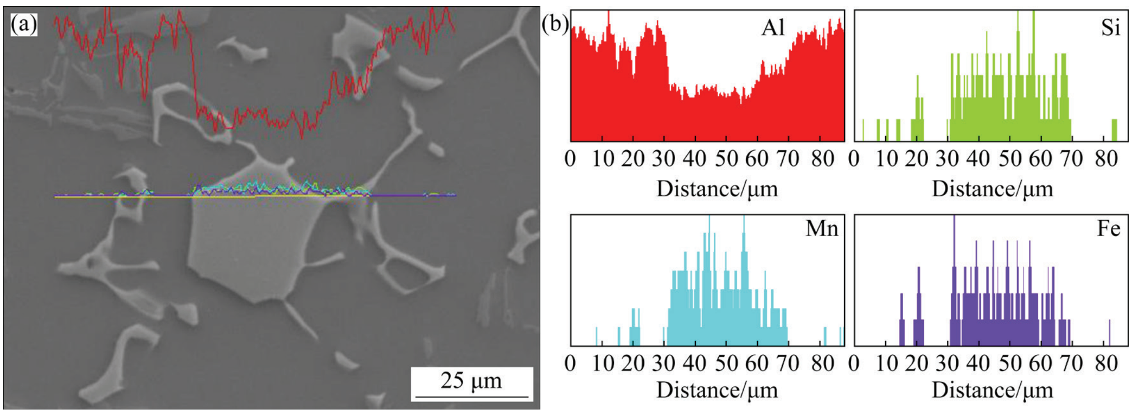


**Fig. 4** SEM image (a) and composition line scan maps (b) of Fe-rich phase with coupled structure

### 3.3 3D morphologies

Figure 6 shows the 3D morphologies of Fe-rich phases in the alloy at different holding temperatures. Independently distributed Fe-rich phases are shown with different colors, while the adjacent and interconnected Fe-rich phases are displayed with the same color. When the holding temperature is 680 °C, a large area in pink is found in the upper part of Fig. 6(a), which is a large-sized Fe-rich phase particle with a span width of ~300 μm. When the holding temperature is reduced to 660 °C, a large light blue area is found on the right side of Fig. 6(b), and its maximum width (~200 μm) is smaller than that of Fig. 6(a) (the pink area). With a further reduction in the holding temperature, the Fe-rich phase shows a continuous distribution, and the pink color disappears (Fig. 6(c)). The size uniformity and distribution of Fe-rich phases in Fig. 6(c) are improved significantly compared with those in Figs. 6(a) and (b).

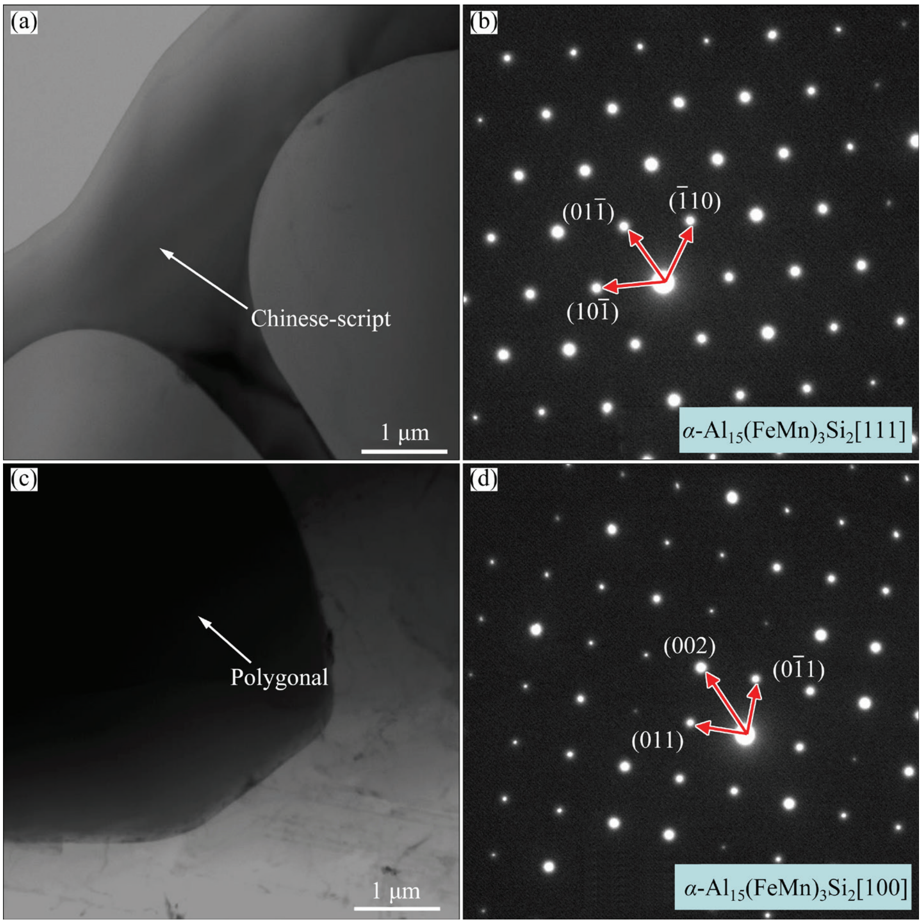


**Fig. 5** Bright-field TEM images (a, c) and SADPs (b, d) of Fe-rich phase in alloy at holding temperature of 630 °C

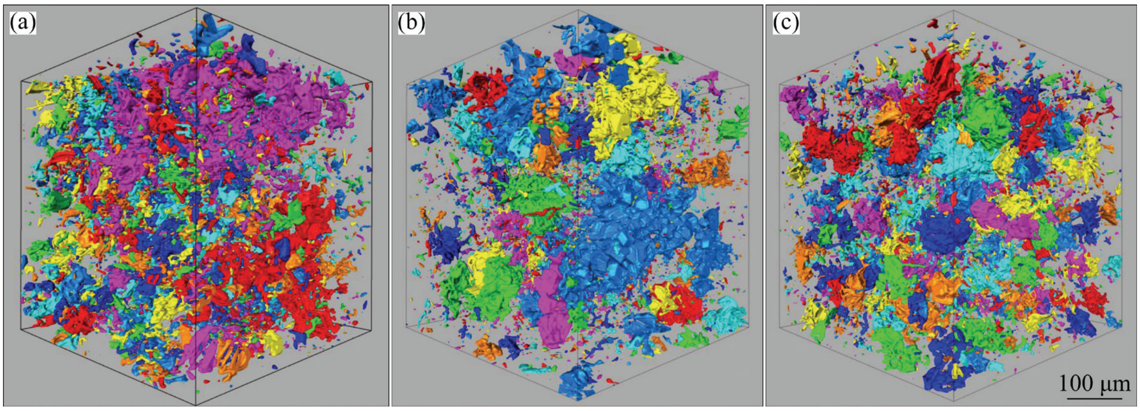


**Fig. 6** Overall 3D morphologies of Fe-rich phases at different holding temperatures: (a) 680 °C; (b) 660 °C; (c) 615 °C

3D morphological characteristic parameters of the Fe-rich phase particles (Fig. 6) are listed in

Table 2. The subvolume of each sample is 0.125 mm$^3$, and the statistical range of the equivalent diameter $D_{eq}$ exceeds 5 μm. With decreasing holding temperature, the number of Fe-rich phases first significantly decreases and then increases slightly when the holding temperature drops to 615 °C. The corresponding number and volume fraction are decreased by 46.3% and 47.6% compared with the counterpart at 680 °C, respectively. After holding at a lower temperature, the $D_{eq}$ of Fe-rich phase particles also decreases, but the sphericity shows no obvious change. It has a closely relationship between $D_{eq}$ and sphericity. In our previous study, we noted that the sphericity of the Fe-rich phase after gravitational sedimentation is inversely proportional to its equivalent diameter [28]. The volume of the largest Fe-rich phase gradually decreases with decreasing holding temperature, but its connectivity is slightly increased at 660 °C due to a reduction in the total volume fraction of the Fe-rich phase. When the holding temperature is 615 °C, the maximum volume of the largest Fe-rich phase and its connectivity are 107243 μm$^3$ and 2.4%, respectively, which decrease by 93.6% and 88.0% compared with those at 680 °C, respectively.

Figure 7 shows the distribution of Fe-rich phases with various morphological characteristics from Fig. 6. The $D_{eq}$ and sphericity distribution of the Fe-rich phases are fitted to the normal function.

**Table 2** 3D morphological characteristic parameters of Fe-rich phases at different holding temperatures (0.5 mm × 0.5 mm × 0.5 mm)

| Holding temperature/°C | Number | Volume fraction/% | Equivalent diameter/μm | Sphericity | Maximum volume/μm$^3$ | Connectivity/% |
|---|---|---|---|---|---|---|
| 680 | 4278 | 6.72 | 10.32±6.63 | 0.68±0.17 | 1684010 | 20 |
| 660 | 2060 | 5.01 | 8.70±7.90 | 0.65±0.16 | 1200530 | 22 |
| 615 | 2298 | 3.52 | 9.30±7.29 | 0.65±0.17 | 107243 | 2.4 |

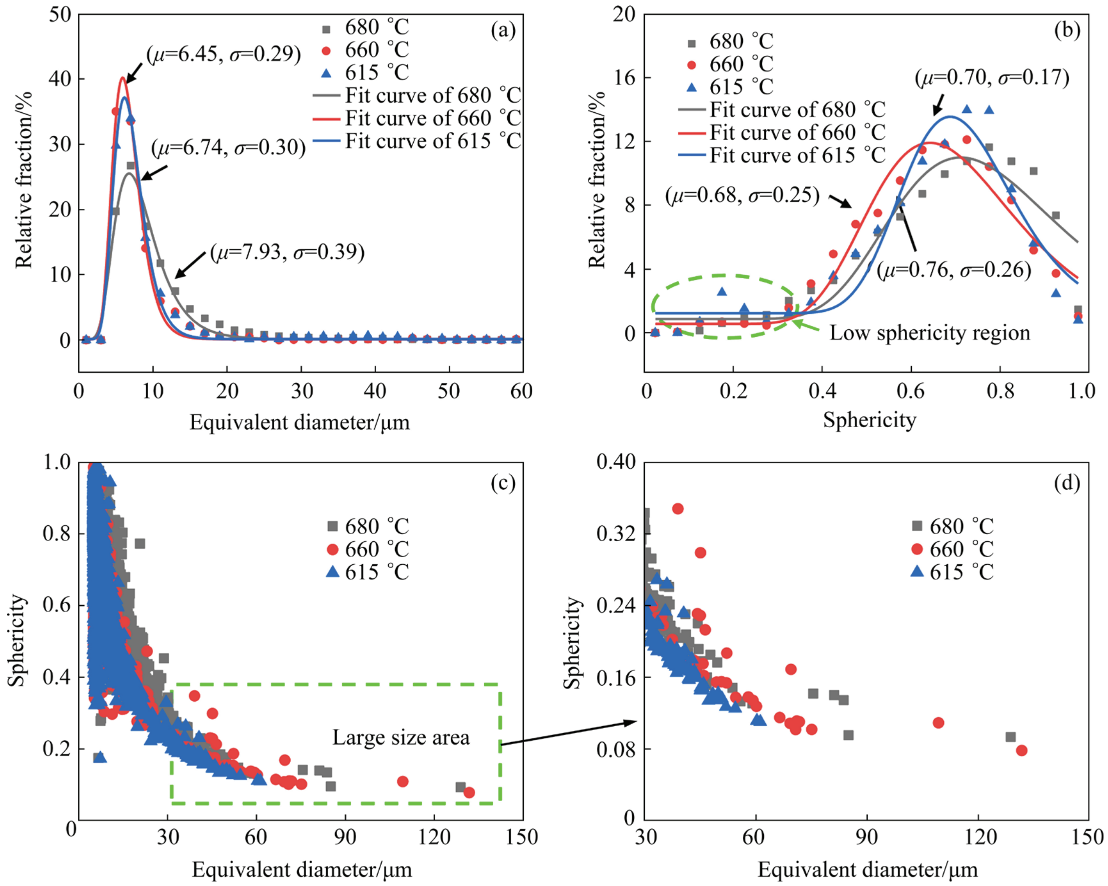


**Fig. 7** Equivalent diameter (a), sphericity (b) distribution and their relationship (c, d) of Fe-rich phases in alloy at different holding temperatures ($\mu$ is the average value, and $\sigma$ is the standard deviation)

Figure 7(a) shows that the average value ($\mu$) and standard deviation ($\sigma$) for the $D_{eq}$ of Fe-rich phases decreased at a lower holding temperature, which means that a smaller size and more uniform Fe-rich phase can be obtained at a lower holding temperature. Figure 7(b) shows that the $\mu$ of the sphericity of the Fe-rich phase slightly decreased, while the $\sigma$ value slightly increased, which indicates that the average shape coefficients of the Fe-rich phases were reduced. However, their distribution concentrations were improved. The distribution uniformity of the Fe-rich phase is consistent with the results in Fig. 2. Figures 7(c) and (d) present the sphericity and $D_{eq}$ of the Fe-rich phases at different holding temperatures. The sphericity and $D_{eq}$ of the Fe-rich phase are mainly distributed in the intervals of 0.3−1.0 and 5−30 μm, respectively. Figure 7(d) shows a partially enlarged view of Fig. 7(c), showing the distribution of particles with a particle size of more than 30 μm. At higher holding temperatures (660−680 °C), some Fe-rich particles more than 60 μm in size appear, while these particles almost disappear in the alloy at 615 °C.

The typical 2D morphologies of the Fe-rich phases in the synchrotron X-ray slice are selected, and then their real 3D morphologies are reconstructed, as shown in Fig. 8. Figures 8(a−c) show the 2D morphologies of the Fe-rich phases in the slices, including star-like, polygonal, individual Chinese-script and coupled structures. Figure 8(d) presents the 3D structure of the star-like Fe-rich phase at 680 °C, which is mainly composed of multiple multibranched, primary Fe-rich phases and derived, irregular, secondary Fe-rich phases. The multibranched structure is composed of six long rods, and these rods with polygonal sections are perpendicular to each other. The length of the above rods reaches 30 μm, and the section width is measured to be 15−20 μm. The surface thickness results show that the primary part of the Fe-rich phase mainly exhibits red and yellow colors, while the secondary part mainly exhibits blue and green colors. This result indicates that the thickness of the primary phases is much greater than that of the secondary phases. It is worth noting that the middle region of the two long rod-shaped primary phases is blue and green, which means that there is a concave or hollow structure. The concave or hollow structure is closely related to the growth process of the primary Fe-rich phase [36,37]. The average curvature of the star-like primary phases is 0.07, which indicates that the concave and convex areas of this structure tend to be balanced. Figure 8(e) shows that the 3D morphology of the polygonal Fe-rich phase at 660 °C is composed of multiple regular polyhedrons and irregular coupled dendrites. These regular polyhedrons with a size range of 15−20 μm are connected to each other, which indicates that these particles agglomerate during melt holding. Compared with the star-like phase, the $D_{eq}$ of the polygonal phase is slightly lower, while the average surface thickness is higher. Figures 8(f, g) show that the 3D structure of the coupled structure is composed of a regular polyhedron and closely connected dendrites, while the individual Chinese-script phase is mainly composed of coupled dendrites. Compared with the star-like and polygonal phases in Figs. 8(d, e), the size of the coupled structure and individual Chinese-script phases is greatly reduced, but the sphericity is significantly improved. In addition, the average surface thickness is significantly decreased, while the average surface curvature is significantly increased, which indicates that the growth of the coupled structure and individual Chinese-script phases is inhibited by more restrictions and has an obvious convex trend.

## 4 Discussion

Figure 9 shows the equilibrium solidification phase diagram of the Al−7.0Si−1.0Fe−Mn alloy. The equilibrium phases mainly include Al, Si and $\alpha$-$Al_{15}(FeMn)_3Si_2$ and $\beta$-$Al_5FeSi$ phases. The precipitation sequence is Liquid → $\alpha$-$Al_{15}(FeMn)_3Si_2$ (615.3−677.1 °C) → $\alpha$-$Al_{15}(FeMn)_3Si_2$ + Al (615.3−577.1 °C) → $\alpha$-$Al_{15}(FeMn)_3Si_2$ + Al + Si (577.1 °C). It is worth noting that the initial formation temperature of the $\alpha$-$Al_{15}(FeMn)_3Si_2$ phase is 677.1 °C. Therefore, the test alloy remains a liquid at 680 °C, and some primary Fe-rich phases are precipitated at 660 °C. These primary Fe-rich phases exhibit fine granularity due to low undercooling. When the holding temperature is 615−645 °C, the coarse primary Fe-rich phases are formed at greater undercooling and settle to the furnace bottom due to gravity.

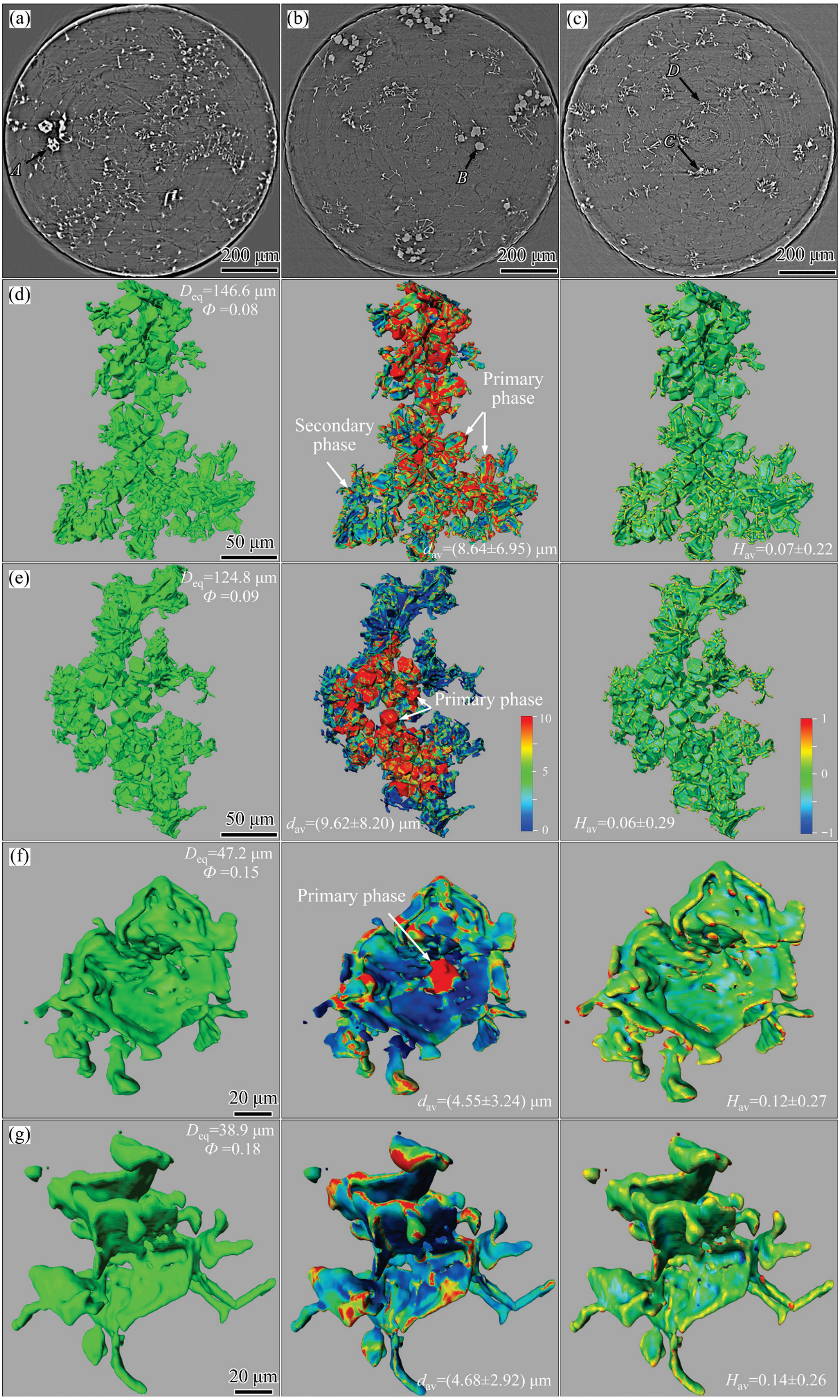


**Fig. 8** Slices (a−c), 3D structure, surface thickness and mean curvature (d−g) of Fe-rich phases at different holding temperatures: (a, d) 680 °C; (b, e) 660°C; (c, f, g) 615 °C

To reveal the growth behavior of primary Fe-rich phases during melt holding, synchrotron X-ray radiography is used to capture in situ solidification images, as shown in Fig. 10. When the cooling time and temperature are 1244 s and 654.2 °C, respectively, three primary Fe-rich phases are clearly observed in the field of view (FOV) of 3.5 mm × 4.5 mm. These primary phases with diameters of 20−30 μm show a granular shape, which is similar to the ones in our previous work [32]. With the extension of cooling time, the number and size of particles increase. However, no more of the Fe-rich phase forms from 1466 to 3246 s. Figure 10(f) shows that two new primary particles are found at the right corner of the FOV at 620.9 °C. The final size of these particles is approximately 60 μm, which is only 15%−25% of the previously formed primary Fe-rich phase. When the cooling time and melt holding temperature are 3618 s and 614.7 °C, respectively, many Fe-rich particles with small sizes are observed in the FOV. These particles are known as secondary Fe-rich phases, which have formation temperatures close to those of the $\alpha$(Al) dendrites.

Therefore, two types of primary Fe-rich phases may be formed during the melt holding process. The first type of primary phase is formed at higher temperatures, which has a coarse size and is prone

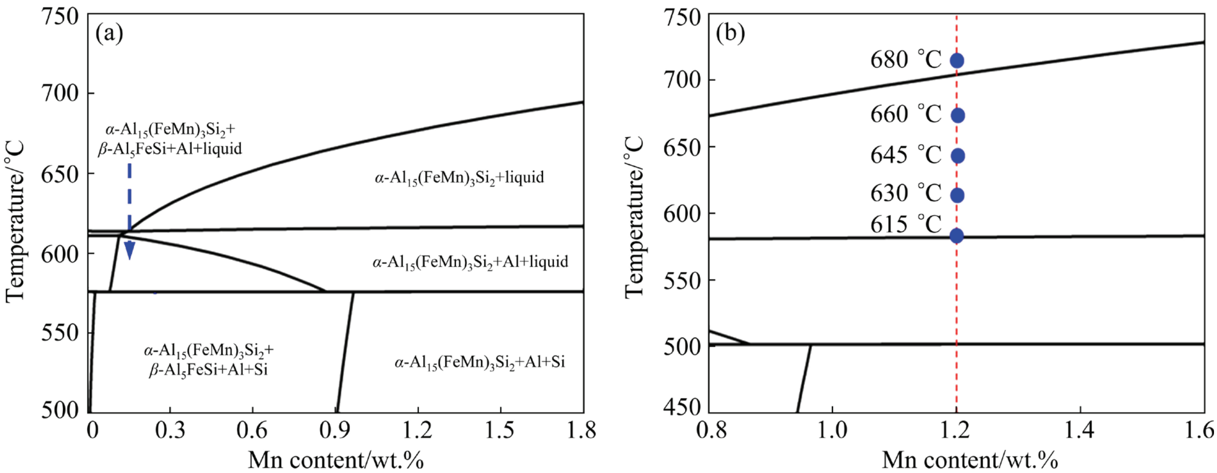


**Fig. 9** Equilibrium solidification phase diagram (a) and corresponding enlarged diagram (b) of Al−7.0Si−1.0Fe−Mn alloy

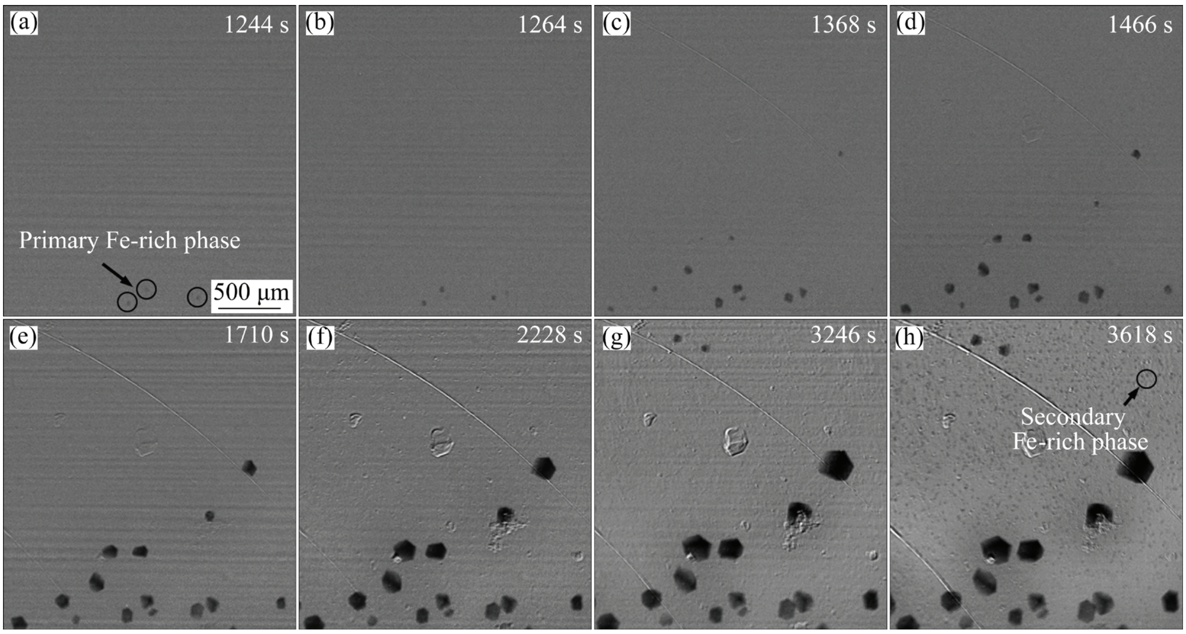


**Fig. 10** Growth and solidification behavior of Fe-rich phase in alloy under near-equilibrium solidification

to sedimentation. The second type of primary phase is formed at relatively low temperatures, which usually shows a coupled structure consisting of regular polyhedrons and Chinese-script phases. The nucleation temperature of these regular polygons is slightly higher than that of $\alpha$(Al), and the growth rate is slow at low undercooling, which results in a typical size no more than 20 μm in the actual casting process. According to Stokes' sedimentation formula, the sedimentation rate of particles is proportional to the square of particle size, that is, fine particles have lower sedimentation rates [22,27]. Therefore, most of the second type of regular polyhedron phases may remain in the melt and agglomerate during the sedimentation process [25]. Moreover, these regular polyhedron phases can act as nucleation sites for the Chinese-script phase in the subsequent solidification process, which promotes the formation of coupled structures [28,34].

Figure 11 shows the growth rate curve of the largest particle in the FOV. The relationship between $D_{eq}$ and the cooling time ($t$) is fitted to the ExpDec1 function:

$$D_{eq}=408.9-954.7\exp(-t/1342) \tag{1}$$

According to Formula (1), it can be inferred that the initial formation time of the Fe-rich phase is approximately 1148 s, and the corresponding temperature of the melt is approximately 655.9 °C. With increasing cooling time, the $D_{eq}$ of the Fe-rich phase gradually increases, but the growth rate gradually decreases. When the cooling time reaches 3400 s, the size of the first type of primary Fe-rich phase shows no obvious change, and the maximum size of the particles is approximately 340 μm. Therefore, the growth time of the primary Fe-rich phase in the Al−7Si−1.0Fe−1.2Mn alloy at a cooling rate of 1 °C/min is approximately 2250 s, which provides reliable data to support Fe removal by natural sedimentation.

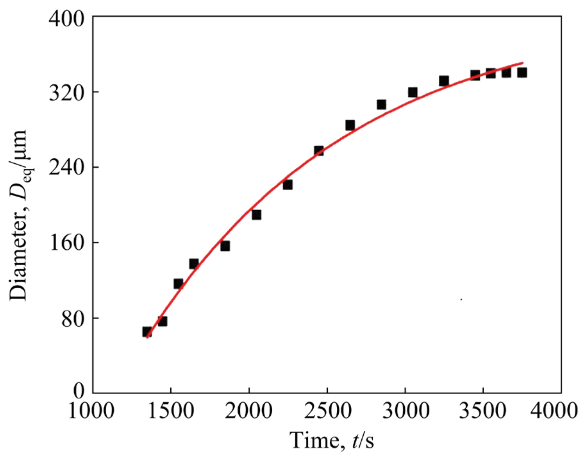


**Fig. 11** Growth rate of Fe-rich phase under near-equilibrium solidification conditions

## 5 Conclusions

(1) The segregation of the Fe-rich phase in Al−7Si−1.0Fe−1.2Mn alloys is significantly improved with decreasing holding temperature, and the 2D morphology undergoes a transformation from a coarse star-like and polygonal shapes to fine Chinese-script shape and coupled structures consisting of Chinese-script and polygonal shapes.

(2) The 3D structure of the star-like Fe-rich phase is mainly composed of multiple multi-branched primary phases and derived irregular secondary phases. The coupled phase is composed of a regular polyhedron and some closely connected dendrites, and the Chinese-script phases are mainly composed of coupled dendrites.

(3) As the holding temperature decreases from 680 to 615 °C, the number and volume fraction of the Fe-rich phase decrease by 46.3% and 47.6%, respectively, and the volume of the largest phase and its connectivity decrease by 93.6% and 88.0%, respectively.

(4) Two types of primary Fe-rich phases may be formed during the cooling and holding process. One is formed at higher temperatures and is prone to sedimentation, the other is formed at lower temperatures and has a regular polygonal shape. The later primary phases usually remain in the melt, agglomerate during holding and act as nucleation sites for coupled structures to form during the subsequent solidification process.

(5) The period for the nucleation and growth of the primary Fe-rich phase is approximately 37.5 min at a cooling rate of 1 °C/min.

### CRediT authorship contribution statement

**Dong-fu SONG:** Conceptualization, Software, Investigation, Visualization, Data curation, Writing − Original draft preparation; **Yu-liang ZHAO:** Validation, Writing − Review and editing; **Yi-wang JIA:** Methodology; **Xin-tao LI:** Formal analysis; **Nan ZHOU:**

Supervision; **Kai-hong ZHENG:** Resources; **Wei-wen ZHANG:** Project administration, Funding acquisition.

## Declaration of competing interest

The authors declare that they have no known competing financial interests or personal relationships that could have appeared to influence the work reported in this paper.

## Acknowledgments

This work was supported by the National Natural Science Foundation, China (No. 52074131), the National Key R&D Project, China (No. 2022YFC3900500), the International Technology Cooperation Program of Guangdong Academy of Sciences, China (No. 2020GDASYL-20200504001), and the Open Competition to Select the Best Candidate of Shangrao, China (No. 2021A005). We would like to thank the BL13HB beamline of Shanghai Synchrotron Radiation Facility (SSRF) for providing synchrotron radiation beamtime (Nos. 2020-SSRF-PT-011937, 2021-SSRF-PT-017645).

## References

[1] RAABE D, PONGE D, UGGOWITZER P J, ROSCHER M, PAOLANTONIO M, LIU Chuan-lai, ANTREKOWITSCH H, KOZESCHNIK E, SEIDMANN D, GAULT B, GEUSER F, DESCHAMPS A, HUTHINSON C, LIU Chun-hui, LI Zhi-ming, PRANGNELL P, ROBSON J, SHANTHRAJ P, VAKILI S, SINCLAIR C, BOURGEOIS L, POGATSCHER S. Making sustainable aluminum by recycling scrap: The science of “dirty” alloys [J]. Progress in Materials Science, 2022, 128: 100947.

[2] LI Ming-yang, GAO Feng, SUN Bo-xue, NIE Zuo-ren. Analysis of carbon emission reduction and carbon emission peak for aluminum production in China based on target scenario [J]. The Chinese Journal of Nonferrous Metals, 2022, 32(1): 148−158. (in Chinese)

[3] YANG Yi, GUO Yao-qi, ZHU Wen-song, HUANG Jian-bai. Environmental impact assessment of China’s primary aluminum based on life cycle assessment [J]. Transactions of Nonferrous Metals Society of China, 2019, 29(8): 1784−1792.

[4] GUTOWSKI T G, SAHNI S, ALLWOOD J M, ASHBY M F, WORRELL E. The energy required to produce materials: Constraints on energy-intensity improvements, parameters of demand [J]. Philosophical Transactions of the Royal Society A: Mathematical Physical and Engineering Sciences, 2013, 371(1986): 20120003.

[5] GRAEDEL T E, HARPER E M, NASSAR N T, RECK B K. On the materials basis of modern society [J]. Proceedings of the National Academy of Sciences of the United States of America, 2015, 112(20): 6295−3000.

[6] DAHMUS J B, GUTOWSKI T G. What gets recycled: An information theory based model for product recycling [J]. Environmental Science and Technology, 2007, 41(21): 7543−7550.

[7] SUBODH K D, JOHN A S G, KAUFMAN J G, EMADI D, MAHFOUD M. Aluminum recycling — An integrated, industrywide approach [J]. JOM, 2010, 62: 23−26.

[8] NAKAJIMA K, TAKEDA O, MIKI T, MATSUBAE K, NAKAMURA S, NAGASAKA T. Thermodynamic analysis of contamination by alloying elements in aluminum recycling [J]. Environmental Science and Technology, 2010, 44(14): 5594−5600.

[9] LIN Bo, ZHANG Wen-xin, ZHENG Xiao-ping, ZHAO Yu-liang, LOU Zhao-hui, ZHANG Wei-wen. Developing high performance mechanical properties at elevated temperature in squeeze cast Al−Cu−Mn−Fe−Ni alloys [J]. Materials Characterization, 2019, 150: 128−137.

[10] HE Xiang-xiang, LIN Bo, FAN Tao, ZHENG Cheng-kun, ZHANG Wei-wen. Effect of iron content on microstructure and mechanical properties of Al−Zn−Mg−Cu alloys prepared by squeeze casting [J]. Transactions of Materials and Treatment, 2021, 42(12): 44−52.

[11] LIN Chong, WU Shu-sen, LÜ Shu-lin, WU He-bao, CHEN Han-xin. Influence of high pressure and manganese addition on Fe-rich phases and mechanical properties of hypereutectic Al−Si alloy with rheo-squeeze casting [J]. Transactions of Nonferrous Metals Society of China, 2019, 29(2): 253−262.

[12] LIU Chao-feng, JIAO Xiang-yi, NISHAT H, AKHTAR S, WIESNER S, GUO Zhi-peng, XIONG Shou-mei. Characteristics of Fe-rich intermetallics compounds and their influence on the cracking behavior of a newly developed high-pressure die cast Al−4Mg−2Fe alloy [J]. Journal of Alloys and Compounds, 2021, 854: 157121.

[13] LIU Xu, WANG Cheng, ZHANG Shao-you, SONG Jia-wang, ZHOU Xiao-li, ZHA Min, WANG Hui-yuan. Fe-bearing phase formation, microstructure evolution, and mechanical properties of Al−Mg−Si−Fe alloy fabricated by the twin-roll casting process [J]. Journal of Alloys and Compounds, 2021, 886: 161202.

[14] LI Zai-dao, LIMODIN N, TANDJAOUI A, QUAEGEBEUR P, WITZ J F, BALLOY D. Influence of Fe content on the damage mechanism in A319 aluminum alloy: Tensile tests and digital image correlation [J]. Engineering Fracture Mechanics, 2017, 183: 94−108.

[15] ZHANG Li-feng, GAO Jian-wei, DAMOAH L N W, ROBERTSON D G. Removal of iron from aluminum: A review [J]. Mineral Processing and Extractive Metallurgy Review, 2012, 33(2): 99−157.

[16] MORAES H L D, OLIVEIRA J R D, ESPINOSA D C R, TENÓRIO J A S. Removal of iron from molten recycled aluminum through intermediate phase filtration [J]. Materials Transactions, 2006, 47(7): 1731−1736.

[17] KIM S W, IM U H, CHA H C, KIM S H, JANG E J, KIM K Y. Removal of primary iron rich phase from aluminum−silicon melt by centrifugal separation [J]. China Foundry, 2013, 10: 112−117.

[18] LI Tian-xiao, XU Zhen-ming, SUN Bao-de, SHU Da, ZHOU Yao-he. Electromagnetic separation of primary Fe-rich phases from aluminum−silicon melt [J]. Transactions of Nonferrous Metals Society of China, 2003, 13(1): 121−125.

[19] YANG Wen-chao, GAO Feng, JI Shou-xun. Formation and sedimentation of Fe-rich intermetallics in Al−Si−Cu−Fe alloy [J]. Transactions of Nonferrous Metals Society of China, 2015, 25: 1704−1714.

[20] BAO Yu, LV Guo-qiang, WANG Yi-bo XIAO Ting, HE Yun-fei, ZHANG Yu-feng, LEI Yun, MA Wen-hui. Simultaneous removal of silicon and Fe-rich phases from coarse Al−Si alloys using manganese under electromagnetic field [J]. Metallurgical and Materials Transactions B, 2018, 49: 3413−3423.

[21] XIAO Ting, LV Guo-qiang, BAO Yu, DUO Wen-chao, XU Long, MA Wen-hui. Electromagnetic separation of coarse Al−Si melts: The migration behavior of Fe-rich phase and continuous growth of primary silicon [J]. Journal of Alloys and Compounds, 2020, 819: 153006.

[22] FLORES A, SUKIENNIK M, CASTILLEJOS A H, ACOSTA F A, ESCOBEDO J C. A kinetic study on the nucleation and growth of the $Al_8FeMnSi_2$ intermetallic compound for aluminum scrap purification [J]. Intermetallics, 1998, 6: 217−227.

[23] CAO X, CAMPBELL J. The solidification characteristics of Fe-rich intermetallics in Al−11.5Si−0.4Mg cast alloys [J]. Metallurgical and Materials Transactions A, 2004, 35(5): 1425−1435.

[24] BECKER H, THUM A, DISTL B, KRIEGEL M J, LEINEWEBER A. Effect of melt conditioning on removal of Fe from secondary Al−Si alloys containing Mg, Mn, and Cr [J]. Metallurgical and Materials Transactions A, 2018, 49(12): 6375−6389

[25] ZHANG Xiao-zu, WANG Dong-tao, NAGAUMI H, WANG Rui, WU Zi-bin, LI Xin-zhong, ZHANG Hai-tao. Highly efficient Fe separation induced by Fe-containing particle agglomeration in Al−7Si−0.3Mg alloy melt [J]. Journal of Materials Research and Technology, 2022, 21: 604−616.

[26] DHINAKAR A, LU P Y, CHEN J K, TANG N K. Iron reduction in 356 secondary aluminum alloy by Mn and Cr addition for sediment separation [J]. International Journal of Metalcasting, 2021, 15(3): 182−192.

[27] SONG Dong-fu, ZHAO Yu-liang, WANG Zhi, JIA Yi-wang, HUANG Hui-lan, ZHANG Da-tong, ZHANG Wei-wen. Effect of Mn/Fe ratio on Fe removal rate and tensile ductility of an Al−7.0Si−2.4Fe alloy [J]. Journal of Materials Research, 2021, 36: 1357−1369.

[28] SONG Dong-fu, WANG Shun-cheng, ZHAO Yu-liang, LIU Shu-hong, DU Yong, KANG Yue-hua, WANG Zhi, ZHANG Wei-wen. Effect of melt holding on the morphological evolution and sedimentation behavior of Fe-rich intermetallic phases in Al−Si−Fe−Mn−Mg alloy [J]. Transactions of Nonferrous Metals Society of China, 2020, 30(1): 1−13.

[29] SONG Dong-fu, JIA Yi-wang, LI Qing, ZHAO Yu-liang, ZHANG Wei-wen. Effect of initial Fe content on microstructure and mechanical properties of recycled Al−7.0Si−Fe−Mn alloys with constant Mn/Fe ratio [J]. Materials, 2022, 15: 1618.

[30] SONG Dong-Fu, ZHAO Yu-liang, WANG Zhi, JIA Yi-wang, LI Dao-xi, FU Ya-nan, ZHANG Da-tong, ZHANG Wei-wen. 3D Fe-rich phases evolution and its effects on the fracture behavior of Al−7.0Si−1.2Fe alloys by Mn neutralization [J]. Acta Metallurgica Sinica (English Letters), 2022, 35: 163−175.

[31] CHEN S L, DANIES S, ZHANG F, CHANG Y A, OATES W A. The PANDAT software package and its applications [J]. Calphad, 2002, 26(2): 175−188.

[32] SONG Dong-fu, ZHAO Yu-liang, JIA Yi-wang, LI Run-xia, ZHOU Nan, ZHENG Kai-hong, FU Ya-nan, ZHANG Wei-wen. Study of the evolution mechanisms of Fe-rich phases in Al−Si−Fe alloys with Mn modification using synchrotron X-ray imaging [J]. Journal of Alloys and Compounds, 2022, 915: 165378.

[33] SONG Dong-fu, ZHAO Yu-liang, JIA Yi-wang, LI Xin-tao, FU Ya-nan, ZHANG Wei-wen. Synergistic effects of Mn and B on iron-rich intermetallic modification of recycled Al alloy [J]. Journal of Materials Research and Technology, 2023, 24: 527−541.

[34] DINNIS C M, TAYLOR J A, DAHLE A K. As-cast morphology of Fe-intermetallics in Al−Si foundry alloys [J]. Scripta Materialia, 2005, 53: 955−958.

[35] YANG Jian. Study of the interaction between impurity elements and segergation mechanism in aluminum molten alloy [D]. Shanghai: Shanghai Jiao Tong University, 2018. (in Chinese)

[36] BJURENSTEDT A, CASARI D, SEIFEDDINE S, MATHIESEN R H, DAHLE A K. In-situ study of morphology and growth of primary $\alpha$-Al(FeMnCr)Si intermetallics in an Al−Si alloy [J]. Acta Materialia, 2017, 130: 1−9.

[37] GAO Tong, HU Kai-qi, WANG Long-shuai, ZHANG Bang-ran, LIU Xiang-fa. Morphological evolution and strengthening behavior of $\alpha$-Al(Fe,Mn)Si in Al−6Si−2Fe−$x$Mn alloys [J]. Results in Physics, 2017, 7: 1051−1054.

# Al−Si−Fe−Mn 合金熔体保温过程中富铁相的三维形态特征和生长行为

宋东福[1,2]，赵愈亮[3]，贾义旺[4]，李新涛[1,5]，周 楠[1]，郑开宏[1]，张卫文[2]

1. 广东省科学院 新材料研究所 广东省金属强韧化技术与应用重点实验室，广州 510650；
2. 华南理工大学 金属材料近净成形国家工程技术研究中心，广州 510641；
3. 东莞理工大学 机械工程学院，东莞 523808；
4. 贵州大学 材料与冶金学院，贵阳 550025；
5. 江西寰球新材料科技有限公司，上饶 334499

**摘 要**：采用扫描电子显微镜、透射电子显微镜、热力学计算和同步辐射 X 射线成像技术研究 Al−7.0Si−1.0Fe−1.2Mn 合金熔体保温过程中富铁相的形态演变和生长行为。结果表明，随着保温温度的降低，富铁相的形态由粗大的星形和多边形状转变成细小的汉字状以及汉字和多边形的耦合结构。富铁相的三维形貌显示，星形富铁相由多个多分支的初生相和衍生的不规则次生相组成；耦合结构由多面体和枝晶组成；单一汉字相则由枝晶组成。随着保温温度的降低，富铁相的数量、体积分数以及最大富铁相的体积和连通性显著降低。原位同步辐射 X 射线结果显示，在凝固过程中形成了两类初生富铁相，其中尺寸较小的初生富铁相保留在熔体中，并成为耦合共晶结构富铁相的形核质点。

**关键词**：保温温度；Al−Si 合金；富铁相；3D 形态演变；同步辐射 X 射线

**(Edited by Wei-ping CHEN)**